

3D bulk-resolved g -wave magnetic order parameter symmetry in the metallic altermagnet CrSb

Mengmeng Long,^{1†} Theodore I. Weinberger,^{1†#} Zheyu Wu,^{1†}
Mads F. Hansen,¹ Ran Tao,¹ Mridul Shrestha,¹ Dave Graf,²
Yurii Skourski,³ F. Malte Grosche,¹ Alexander G. Eaton^{1*}

¹Cavendish Laboratory, University of Cambridge,

JJ Thomson Avenue, Cambridge, CB3 0US, UK

²National High Magnetic Field Laboratory, Tallahassee, Florida 32310, USA

³Hochfeld-Magnetlabor Dresden (HLD-EMFL), Helmholtz-Zentrum
Dresden-Rossendorf, Dresden, 01328, Germany

[†]These authors contributed equally to this work.

#tiw21@cam.ac.uk

*alex.eaton@phy.cam.ac.uk

January 22, 2026

Electronic phases of matter, such as magnetism and superconductivity, are defined and distinguished by their order parameters that quantify the spontaneous symmetry breaking underlying each phase. The simplest cases are the uniform magnetisation of ferromagnets^{1,2} and isotropic gap function of conventional superconductors.³ Unconventional superconductors⁴ often have a nodal gap function, where the gap changes sign at nodes on the Fermi surface. This concept of unconventional or nodal order parameter symmetry has recently been extended to numerous magnetic systems,^{5–8} including altermagnets,^{9–13} in which up- and down-spin species are non-degenerate around the Fermi surface. Here we demonstrate that magnetic quantum oscillation¹⁴ measurements can provide a direct, bulk-sensitive, 3D mapping of the order parameter in an unconventional magnet. By rotating a magnetic field through high- and low-symmetry directions of the CrSb Brillouin zone, we show that this material's altermagnetic band structure leads to the loss of mirror symmetry for each spin-split Fermi sheet away from highly symmetric nodal orientations. In momentum space, the difference between up and down spins follows the profile of the $\mathcal{Y}_4^{-3} = zy(3x^2 - y^2)$ spherical harmonic – analogous to a *g*-orbital of the hydrogen atom. While notoriously difficult to resolve in unconventional superconductors, our work demonstrates that the order parameter symmetry of unconventional magnets can be conclusively determined through quantum-oscillatory quasiparticle spectroscopy. Our results empirically establish CrSb as a prototypical *g*-wave metallic altermagnet, which in pristine form possesses low residual resistivities down to $\sim 1 \mu\Omega\text{cm}$, opening numerous avenues for next-generation spintronic device applications.¹⁵

Symmetry properties underpin myriad fundamental aspects across the physical sciences. One poignant example dates from the dawn of quantum mechanics a century ago, when Erwin Schrödinger formulated his wave mechanical description of the hydrogen atom.¹⁶ By considering the spherical symmetry of the Coulomb potential, he demonstrated that the angular component of an electron's wavefunction is described by the Laplacian operator on the unit sphere. This underlies the spherical harmonic description of atomic orbitals, of the form $\mathcal{Y}_l^m(\theta, \varphi)$, providing the first rigorous physical explanation for the discrete quantum numbers that define the architecture of the periodic table.

The breaking of symmetries can lead to profound physical effects. For example, the Anderson-Higgs mechanism^{17,18} specifies how the spontaneous breaking of a local $U(1)$ gauge symmetry allows a massless gauge field to acquire mass. This result has far-reaching consequences, underpinning both the origin of elementary particles as well as enabling the perfect expulsion of magnetic flux from a solid. In a superconductor, this symmetry is broken when the electron fluid condenses into a coherent macroscopic state, thereby locking the phase and rendering the photon massive, which manifests as the Meissner effect. Unconventional superconductors⁴ are those in which the momentum-dependent superconducting energy gap $\Delta(\vec{k})$ changes sign. Typically, this involves the pair-wavefunction possessing lower symmetry than that of the underlying crystal lattice. A hallmark of such additional symmetry breaking is the emergence of a nodal gap structure in reciprocal space, where $\Delta(\vec{k})$ vanishes at specific points or lines on the Fermi surface.

In general, despite the arsenal of experimental probes the modern condensed matter physicist has to hand, it remains stubbornly challenging to conclusively determine the symmetry of $\Delta(\vec{k})$ for a given unconventional superconductor. However, decades of careful measurements have robustly demonstrated that the order parameter symmetry of high- T_c cuprates is of d -wave character,⁴ while superfluid ^3He is p -wave.¹⁹ These designations correspond to symmetries

of spherical harmonics possessing angular momenta $l = 2$ and $l = 1$, respectively – hence this nomenclature for labelling the symmetry properties of the order parameter by analogy to $s, p, d \dots$ atomic shells.

Unconventional magnetism

These concepts of nodal, or unconventional, order parameter symmetries have recently been extended to magnetic systems.^{5,6} Consider the two traditional examples of collinear magnetic order: ferromagnets,^{1,2} in which all spins point in the same direction, and antiferromagnets,²⁰ in which the spin polarisation alternates up and down from site to site. A ferromagnet can be thought of as an s -wave magnet, in which the Fermi surface is separated into unequal portions of majority and minority carriers. Continuing our analogy with superconductors, here $\Delta(\vec{k})$ may be thought of as the difference between up-spins and down-spins, which for a ferromagnet is isotropic in \vec{k} , as is the gap magnitude in conventional s -wave BCS superconductors.

Newly-classified¹⁰ altermagnets are collinear and magnetically compensated like antiferromagnets, but here the spin polarisation alternates in momentum space between opposite \vec{k} -points in the Brillouin zone due to specific crystal and magnetic symmetries that combine time-reversal and spatial operations.^{9–13} In an antiferromagnet, the magnetic structure can be decomposed into two magnetic sublattices, resulting in a doubling of the magnetic unit cell²¹ under a simple translation. Combined with a time-reversal operation, this maps one spin to its opposite counterpart in real space, giving rise to spin-degenerate bands in momentum space. In contrast, an altermagnet requires a point-group operation (such as a rotation, mirror, or screw axis), combined with translation and time-reversal, to interchange opposite spin directions. As a result, altermagnets break Kramers spin-degeneracy and exhibit momentum-dependent spin splitting in their electronic band structures, despite possessing zero net magnetisation – representing a new paradigm of collinear magnetism that bridges conventional ferromagnetism and antiferro-

magnetism.²² This enables, in principle, the manifestation of higher-order even-parity order parameter symmetries (e.g. $d-$, $g-$, $i-$ wave).

In addition to the fundamental interest this new class of magnetic ordering has generated, altermagnets are also predicted to have substantial practical impact. Their ability to efficiently generate and detect spin currents, combined with intrinsic immunity to stray magnetic fields due to their compensated spin structure, makes altermagnets highly promising for future spintronic, neuromorphic computing, and magnetic memory technologies.¹⁵

The search to confirm altermagnetic ordering

Numerous altermagnet candidates have been identified from *ab initio* calculations.^{9, 10, 15, 23, 24} However, most of these are semiconducting or insulating, whereas only a few metallic altermagnet candidates have so far been reported. The realisation of a metallic altermagnet is particularly desirable for efficient charge transport in technological device settings.²⁴ Of the handful of metallic altermagnets predicted by *ab initio* searches, the rutile oxide RuO₂ quickly arose as an especially promising candidate.

However, although early studies of this material reported numerous phenomena that would be consistent with altermagnetic ordering, these results later proved controversial. Firstly, muon spin rotation measurements did not resolve the presence of any static magnetic moments,^{25, 26} in stark contrast to prior neutron and x-ray scattering studies.^{27, 28} Magnetic quantum oscillation measurements by the de Haas-van Alphen effect¹⁴ mapped the bulk electronic band structure,²⁹ which showed a pronounced disagreement with earlier ARPES measurements, instead agreeing well with paramagnetic Fermi surface simulations computed by density functional theory (DFT).^{30, 31} ARPES measurements from two independent groups identified the presence of surface states with an anomalous Rashba-like spin-splitting, of a likely topological character.^{32, 33} These exotic phenomena, confined within a shallow surface layer, could account for the previous

misattribution of seemingly smoking-gun experimental signatures of bulk altermagnetism, with RuO₂ now seemingly established to be paramagnetic in character. Therefore, to robustly confirm the existence of altermagnetic ordering in the solid state, the utilisation of a bulk-sensitive diagnostic tool is imperative.

Symmetry-enforced Kramers spin-degenerate nodal planes

CrSb crystallises in the hexagonal P6₃/*mmc* NiAs-type structure, with chromium atoms stacked along the crystallographic *c*-axis in octahedrally coordinated layers, while the antimony atoms fill the interstitial sites in a trigonal prismatic arrangement³⁴ (Fig. 1a,b). Below a Néel temperature of around 740 K (see Extended Data Fig. 1), the chromium sites possess alternating magnetic moments oriented along the *c*-axis.³⁵ The trigonal arrangement of antimony necessarily requires a 6₃ screw rotation to map a spin-up chromium site to its spin-down counterpart. Therefore, CrSb breaks both pure time-reversal and lattice-translation symmetries, but preserves the combined symmetry involving this spatial operation (of screw rotation and translation) followed by time-reversal. These symmetry properties motivate the proposal that CrSb is a metallic altermagnet.^{10,13,24,36,37}

Kramers' theorem³⁸ states that in time-reversal symmetric systems, single-particle energy levels are at least doubly-degenerate for half-integer spins. In ferromagnets, the broken time-reversal symmetry implied by the magnetic order causes band state energies to be spin-split, causing the formation of distinct majority- and minority-spin Fermi surface pockets. By contrast, up- and down-spin band states remain degenerate in collinear antiferromagnets, because the up- and down-spin sites in real space can be connected by a combined time-reversal operation and a spatial translation (or inversion). The distinguishing feature of *altermagnets* is that up- and down-spin sites in real space are not mapped onto each other by inversion or translation, which causes the up- and down-spin states in reciprocal space no longer to be de-

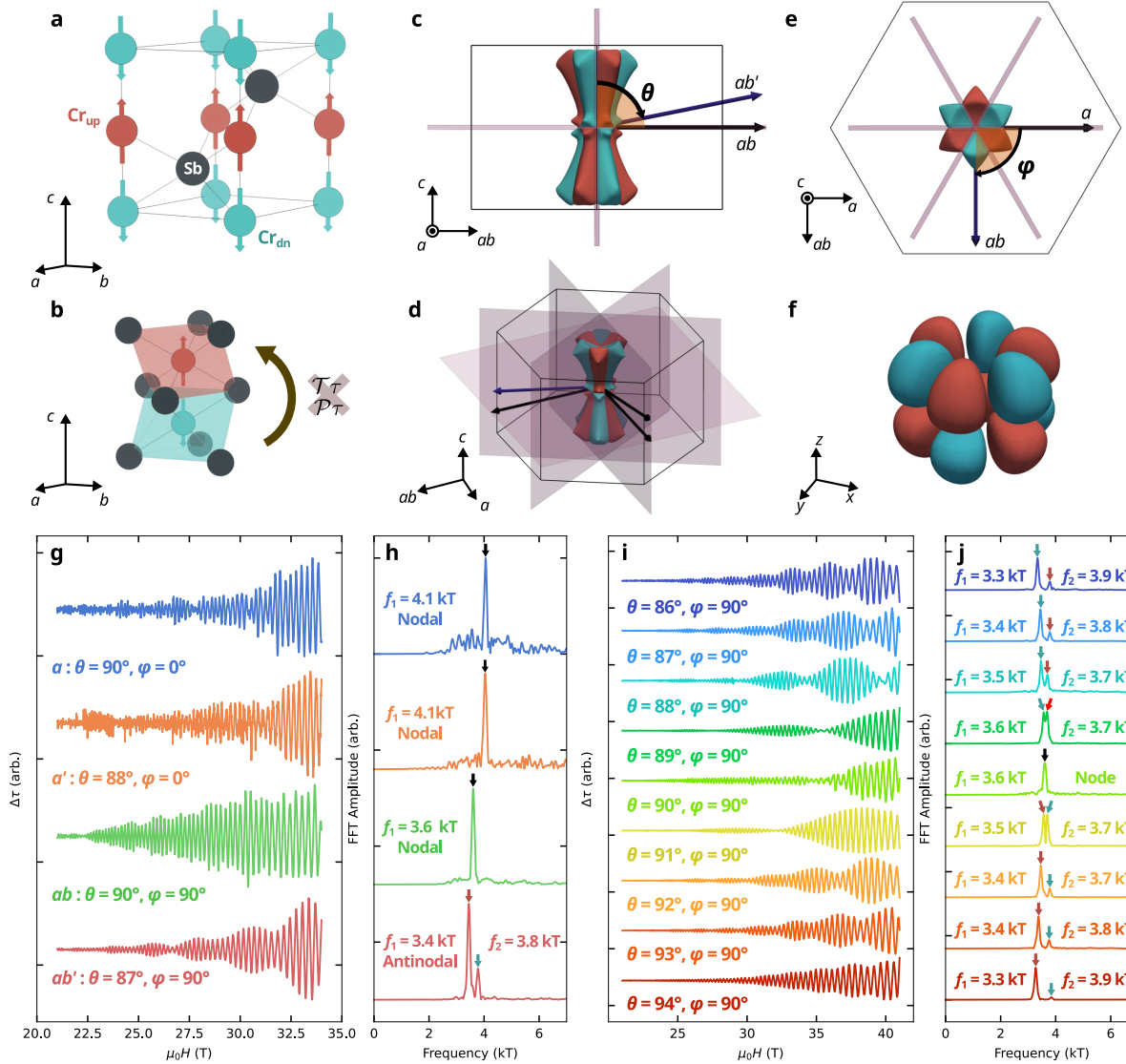


Fig. 1. Nodal planes bisect g -wave-symmetric spin-split Fermi surface sheets in CrSb. **a**, The crystal structure of CrSb, with alternating magnetic moments on the Cr sites oriented along the c -axis. Red indicates spin-up, with blue corresponding to spin-down. **b**, The trigonal arrangement of the antimony ions means that the mapping of a red chromium site to a blue one cannot be performed by translation and time-reversal operations alone, but necessarily requires a screw rotation, which is a point-group operation. **c-e**, The primary Fermi surface sheet of CrSb is a closed 3D ellipsoidal pocket, shaped like a dogbone. Here we indicate its spin-split character with red and blue colouring, with the distinctive g -wave flowerlike symmetry of the order parameter visible looking along the c -axis. Nodal planes – where spin degeneracy is imposed by symmetry – are given by thin shaded slabs, bisecting the Fermi surface where the up- and down-spin sheets cross. Here we introduce the azimuthal angle φ defined as the inclination from a to ab , i.e. from [100] towards [110], and the polar angle θ from c towards the ab plane, i.e. from [001] to [100] or equivalently [001] to [110]. **f**, Visual depiction of the $\mathcal{Y}_4^{-3} = zy(3x^2 - y^2)$ real spherical harmonic, which characterises the g -wave symmetry profile of

Fig. 1. (cont.) altermagnetic spin-splitting in CrSb. **g**, Quantum oscillations in the background-subtracted magnetic torque $\Delta\tau$, rescaled to the same maximal amplitude for ease of presentation (see *Methods* for experimental and analytical details) collected at magnetic field \mathbf{H} orientations as indicated, and **h**, their fast Fourier transform (FFT) frequency spectra. A singular FFT peak is observed in the three nodal orientations, which splits into two peaks in the antinodal plane (red data). All measurements were performed at 0.4 K. **i,j** $\Delta\tau$ and corresponding FFT spectra for small rotations of θ in the antinodal plane away from the *ab* direction towards *c*. For \mathbf{H} aligned along *ab*, only one frequency is observed, which elsewhere splits into two distinct peaks. Once \mathbf{H} has rotated by just 4° away from *ab* towards *c*, these two frequency components are separated by a considerable 0.6 kT. The waveforms themselves exhibit a pronounced beating structure, which is acutely sensitive to small modulations of θ .

generate apart from certain high-symmetry points or directions. This could be termed ‘lifted Kramers degeneracy’ in reciprocal space. The symmetry properties of an altermagnet require that $\Delta(g\vec{k}) = -\Delta(\vec{k})$, where $\Delta(\vec{k})$ is hereafter defined to be the spin-splitting of a given Fermi pocket and g is the relevant composite symmetry operation that connects spin sublattices (in CrSb, this is a 6_3 screw rotation plus time-reversal). This implies nodal planes in momentum space where $\Delta(\vec{k}) = 0$, in which spin-degeneracy is enforced by symmetry.

Magnetic quantum oscillation¹⁴ (QO) experiments can identify these nodal planes because $\Delta(\vec{k})$ does not just go to zero for \vec{k} on a nodal plane – it is also mirror-symmetric about the plane. Magnetic fields applied in directions lying within a nodal plane, therefore, yield QO orbits for up- and down-spin Fermi surface sheets that are different, but can be mapped onto each other by a mirror operation about the nodal plane, and which therefore enclose the same area. This leads to a single QO frequency per Fermi pocket for fields in nodal planes. By contrast, for fields oriented away from nodal planes, the up- and down-spin Fermi surface sheets are not related by any symmetry operation, and therefore generally enclose different areas, leading to two distinct QO frequencies. The exception to the latter scenario is when the field is applied perpendicular to a nodal plane, thereby inducing quasiparticle orbits that are parallel to the nodal plane. Orbit

that lie within the nodal plane are truly degenerate, whereas those that lie above the nodal plane will have area-degenerate orbits of opposite spin-texture below the plane (see Extended Data Fig. 8).

The power of using QOs for probing metallic altermagnets is that by measuring for magnetic field orientations in both nodal and antinodal planes we can map the complete order parameter symmetry, $\Delta_i(\theta, \varphi) = [\vec{k}_{F\perp_i}^{\text{up}}(\theta, \varphi) - \vec{k}_{F\perp_i}^{\text{dn}}(\theta, \varphi)]$, in field-angle space. The measurement directly resolves the difference in spin-split frequencies, corresponding to a Fermi wavevector k_F of band index i . This allows us to determine *both* the magnitude of the splitting *and* the exact order parameter symmetry of our spin-splitting function $\Delta(\theta, \varphi)$.

Throughout this article, we shall refer to rotations of the orientation of an applied magnetic field \mathbf{H} through azimuthal angles φ defined in the crystallographic ab plane, and polar angles θ between c and the ab plane (Fig. 1c,e). Note that the a direction is equivalent to b . The $c - a$ plane is a highly symmetric nodal plane in which Kramers degeneracy is enforced by symmetry, while $c - ab$ is antinodal, in which Kramers' theorem is only symmetry-enforced at c and ab – that is, for the real space [001] and [110] directions. In CrSb, g -wave splitting should result in nodal planes every $\theta = 60^\circ$ for rotations in the $a - ab$ plane, and every $\varphi = 90^\circ$ when rotating in the $c - ab$ plane. We also expect to observe truly degenerate orbits when the magnetic field is applied along either the c or ab directions, which are perpendicular to the nodal planes.

We present the experimentally deduced main Fermi surface pocket of CrSb, with its high-symmetry nodal planes between up and down sheets, in Fig. 1c-f. In Fig. 1g, we plot background-subtracted magnetic torque $\Delta\tau$ as a function of magnetic field, to focus on the oscillatory component due to the de Haas-van Alphen effect, measured by cantilever beam magnetometry (see *Methods*). The blue waveform was measured for $\mathbf{H} \parallel a$ at $\theta = 90^\circ, \varphi = 0^\circ$, with the orange data collected a small rotation away in the $c - a$ plane to $\theta = 88^\circ, \varphi = 0^\circ$. The corresponding fast Fourier transform (FFT) spectra in panel h for both of these orientations exhibit a singular

frequency peak at 4.1 kT.

Altermagnetically lifted spin degeneracy

Let us now contrast this with the case of fields in the $c - ab$ (antinodal) plane. The green curve of Fig. 1g was obtained for $\mathbf{H} \parallel ab$ (i.e. $\theta = 90^\circ, \varphi = 90^\circ$), with a monofrequency profile of 3.6 kT. Upon a small θ rotation of 3° towards c , a distinct beat pattern emerges (red curve), with two peaks clearly resolved in the frequency spectra. This is characteristic of the Fermi surface becoming spin-split into two non-degenerate sheets – one spin-up and the other spin-down.

Fig. 1i,j tracks the split peak structure for fields close to the ab direction. Incrementing θ in 1° steps through the $c - ab$ plane for rotations in either direction away from ab (that is, towards $\pm c$), we find that the singular on-axis peak of 3.6 kT clearly splits into two distinct frequency branches, which by 4° of rotation are separated by 0.6 kT. This is reflected in the profile of the waveforms themselves, which exhibit a pronounced beat structure, becoming more pronounced as \mathbf{H} is rotated away from ab towards c by only a few degrees.

The full angular profiles of quantum oscillatory frequency spectra in CrSb for fields in the $c - a$ (nodal) and $c - ab$ (antinodal) planes are shown in Fig. 2. The QO frequency is directly proportional to the extremal area in reciprocal space that is enclosed by a quasiparticle's cyclotron orbit about the Fermi surface cross-section \mathcal{A}_\perp normal to \mathbf{H} , by the Onsager relation $f = (\hbar/2\pi e)\mathcal{A}_\perp$.^{39,40} We indicate how QO frequency maps to reciprocal space area (in inverse squared angstroms, \AA^{-2}) and compare with simulated QO frequency spectra from DFT calculations (see *Methods* for details). The central Fermi sheet of CrSb is a closed ellipsoidal pocket of hole character, shaped like a dogbone. It exhibits QO frequencies of 4.1 kT for $\mathbf{H} \parallel a$ and 3.6 kT for $\mathbf{H} \parallel ab$ (see Extended Data Fig. 3 for additional Fermi surface renderings). Two other bands of electron character also cross the Fermi level, leading to another more geometrically complex Fermi sheet, which possesses a web-like shape (see Fig. 2). The web sheet produces a very

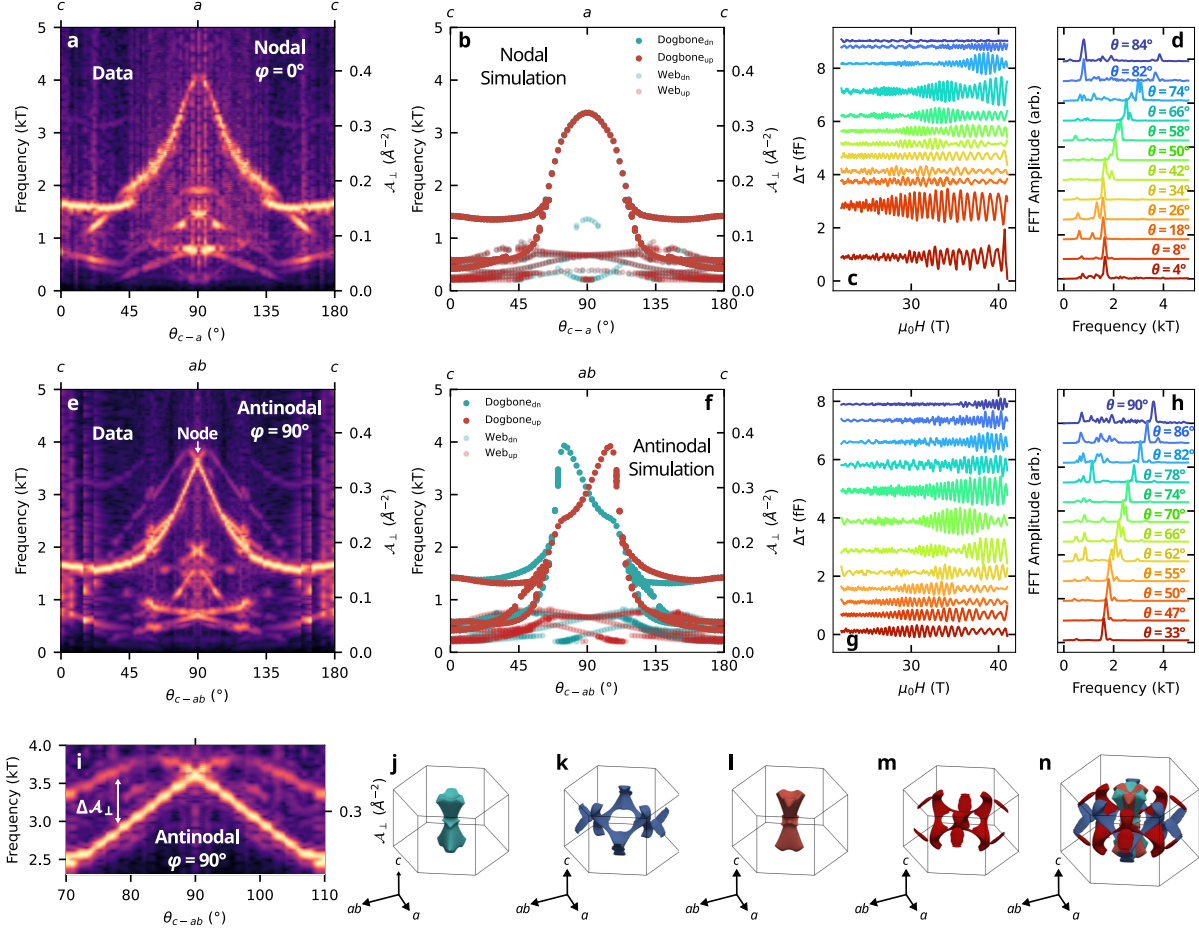


Fig. 2. Mapping the altermagnetically spin-split Fermi surface of CrSb. **a**, Heatmap of the spectral intensity of quantum oscillatory frequencies versus rotation angle in the nodal $c - a$ plane and **b**, simulated frequency profile from DFT calculations (see *Methods*). \mathcal{A}_\perp denotes the enclosed reciprocal space area of a given frequency component. **c,d** Selected $\Delta\tau$ curves and normalized FFTs that contributed to the heatmap in **a** (see Extended Data Fig. 4 for the full $\Delta\tau$ dataset). All data were collected at 0.4 K. **e**, Data and **f**, Simulation for the antinodal $c - ab$ rotation plane, with waveforms and normalised FFTs in **g,h** (and full datasets in Extended Data Fig. 5). Here spin-splitting between non-degenerate Fermi sheets is predicted by the simulation, which is clearly resolved experimentally close to $\theta = 90^\circ$. In **i**, we present a zoomed-in view having high-pass filtered the raw data, to clearly show the non-degenerate spin-up and -down frequency branches crossing the nodal plane at $\theta = 90^\circ$, which are separated by ~ 1 kT. **j,k** Fermi surface rendering of the spin-down sheets of the dogbone and web pockets and **l,m** their spin-up counterparts. **n**, The full Fermi surface of CrSb, including all spin-up and spin-down sheets.

complicated dependence of QO frequency on angle in the low frequency range $\lesssim 2$ kT. Away from nodal planes, the web is also split into up and down sheets, but its geometrical complexity makes this more difficult to resolve than in the case of the dogbone. We therefore predominantly focus on the dogbone for \mathbf{H} oriented close to a or to ab , which produces QO orbits with frequencies $\gtrsim 3$ kT, well above those from the web.

Symmetry-enforced spin degeneracy causes the QO frequencies arising from both the spin-up and spin-down Fermi sheets to be the same for fields in the nodal $c - a$ plane, as depicted by our simulation (Fig. 2b), which qualitatively captures the main features of the data (Fig. 2a). By contrast, for fields in the antinodal $c - ab$ plane, a large splitting of the QO frequencies should occur over the approximate angular interval $60^\circ < \theta < 120^\circ$ (Fig. 2e,f), before the geometric profile of the dogbone leads to an accidental degeneracy. This is exactly what we observed in Fig. 1i,j and is clearly visible in the spectral intensity near $\theta = 90^\circ$ in Fig. 2e. In Fig. 2i we present a zoom-in of this region, to focus on this spectral range. The overlap of frequencies at $\mathbf{H} \parallel ab$, which is abruptly split upon incrementing θ , is characteristic of the altermagnetic lifting of spin degeneracy, indicating two spin-split dogbone Fermi surface sheets (Fig. 2j,l) as predicted by our DFT simulation (Fig. 2f). The considerable difference between frequency branches in Fig. 2i, of ~ 1 kT (corresponding to ~ 0.1 Å⁻²), therefore constitutes a direct observation of altermagnetic spin-splitting throughout the bulk of a material.

Spin-split Fermi surface sheets

In order to track the spin-splitting of the CrSb Fermi surface away from its nodal planes, we measured QOs in a tilted plane of rotation, chosen such that an arc of low symmetry would connect two symmetry-enforced nodal orientations. Along this arc, the spin-splitting should be considerable, but collapse to yield monofrequency waveforms at the nodal orientations. We experimentally performed this by first rotating the sample platform by 14° orthogonally to the axis

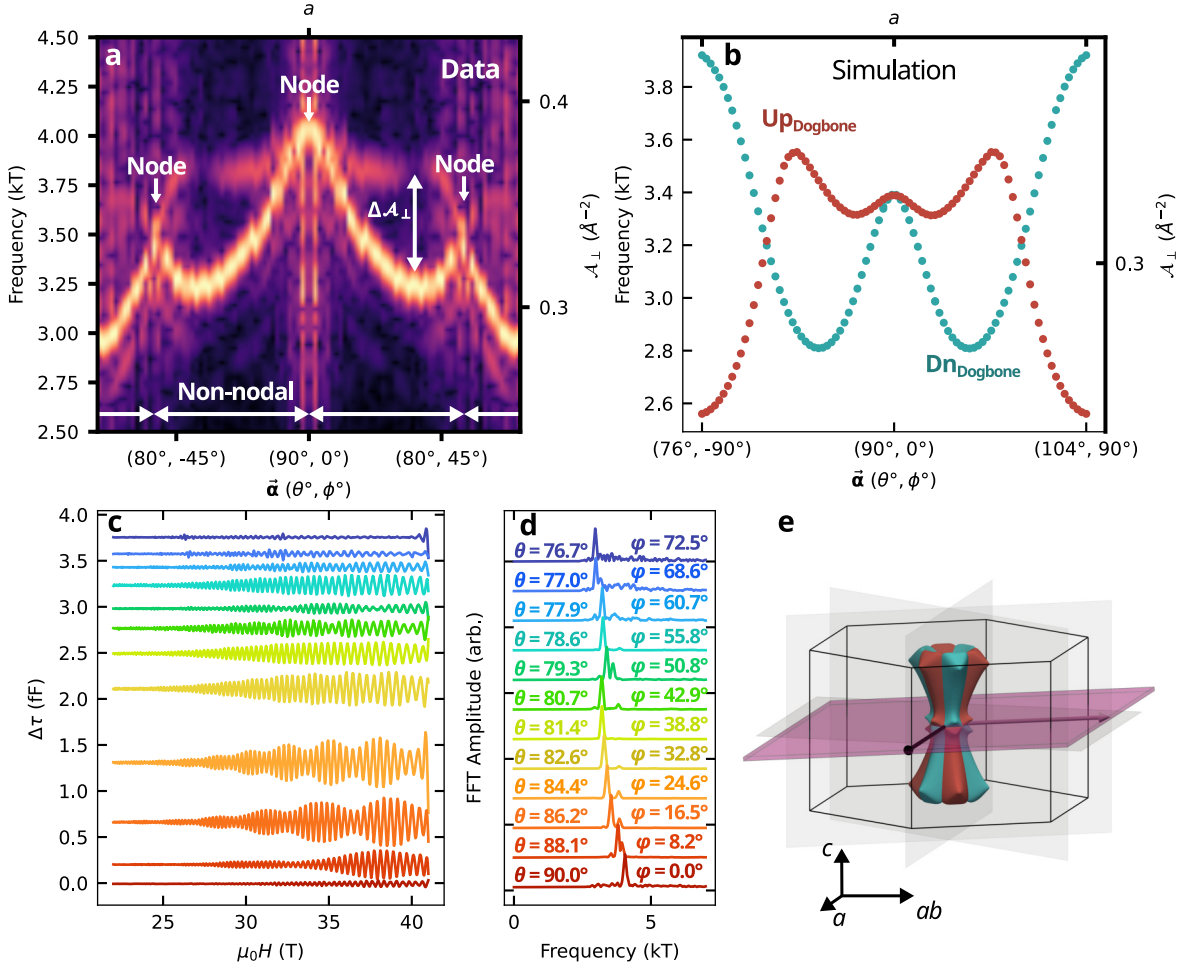


Fig. 3. Confirmation of g -wave altermagnetic spin texture in CrSb. **a**, Heatmap of quantum oscillation frequencies versus rotation angle and **b**, simulated spin-up (red) and spin-down (blue) angular frequency profile computed by DFT. Here we rotate by an angle α through a plane of low symmetry at a tilt of 14° from the ab plane, which is depicted in Extended Data Fig. 2. α is defined such that $\cos(\theta) = \sin(14^\circ) \sin(\alpha)$ and $\tan(\varphi) = \cos(14^\circ) \tan(\alpha)$. Symmetry-enforced nodal planes are crossed at $\varphi = 0^\circ$ and at $\varphi = \pm 60^\circ$. At all other orientations in this low-symmetry plane, significant spin-splitting is observed. **c,d**, Selected $\Delta\tau$ curves and corresponding FFTs that contributed to the heatmap in **a** (the full dataset is presented in Extended Data Fig. 6). **e**, The tilted rotation plane through which \mathbf{H} was swept, whereby the arc that is traced out crosses a nodal plane every 60° increment of φ , due to the g -wave symmetry profile.

of the solenoid before loading it into the magnet. Then we rotated *in-situ* through a polar angle of rotation (labelled α in Fig. 3) that is orthogonal to \mathbf{H} but always at a tilt of 14° relative to the sample holder. This setup means that \mathbf{H} may still be oriented along a , but subsequent rotation of the sample holder increments θ (between $c - a$) and φ (between $a - ab$), in the reference frame of the crystal, such that $\cos(\theta) = \sin(14^\circ) \sin(\alpha)$ and $\tan(\varphi) = \cos(14^\circ) \tan(\alpha)$ (see Extended Data Fig. 2 for further details). We plot the resulting data for these rotational measurements in Fig. 3, including the simulated up- and down-sheet frequency profiles computed from DFT.

The correspondence between experimental observation (Fig. 3a) and theoretical prediction (Fig. 3b) is excellent. A singular frequency peak is observed for $\mathbf{H} \parallel a$ ($\theta = 90^\circ, \varphi = 0^\circ$ in Fig. 3d), giving a bright spot at the nodal location of $\varphi = 0^\circ$ in Fig. 3a. Upon incrementing α , this then splits into two distinct branches, which, within resolution, come back together again close to $\varphi = \pm 60^\circ$ as the next nodal plane is crossed, in close agreement with the simulation.

We determined the effective carrier masses on the two spin-split surfaces in a Lifshitz-Kosevich temperature dependence study of the QO amplitude in this rotation plane at $\alpha = 22^\circ$, which in the reference frame of the crystal corresponds to \mathbf{H} aligned at $\theta = 84.8^\circ, \varphi = 21.4^\circ$ (Fig. 4a). Two peaks are clearly resolved, with $f_1 = 3.41$ kT and $f_2 = 3.82$ kT. Fitting the temperature-dependent oscillatory damping to Lifshitz-Kosevich theory⁴⁰ yields effective masses $m_1^* = 1.97(5) m_e$ and $m_2^* = 2.09(5) m_e$, where m_e is the bare electron mass. For two QO frequency branches that are spin-split daughters of the same mother sheet, the daughters are expected to share the same Fermi velocity $v_F = \partial \varepsilon_k / (\hbar \partial k_\perp)$, where ε_k denotes the quasiparticle dispersion and dk_\perp is oriented locally orthogonal to the Fermi surface. The QO mass is given by $m^* = (\partial \mathcal{A}_\perp / \partial \varepsilon) \hbar^2 / (2\pi)$, where $\partial \mathcal{A}_\perp / \partial \varepsilon = (\partial \mathcal{A}_\perp / \partial k_\perp) / (\hbar v_F)$. If the orbit area scales with the square of the orbit size, $(\partial \mathcal{A}_\perp / \partial k_\perp) \propto \sqrt{\mathcal{A}_\perp}$, with \mathcal{A}_\perp in turn \propto the associated QO frequency. We would therefore expect $m_1^* / m_2^* = \sqrt{f_1 / f_2}$. This is indeed what we observe: $m_1^* / m_2^* = 0.94 \pm 0.04 \simeq \sqrt{f_1 / f_2} = 0.945$, providing strong

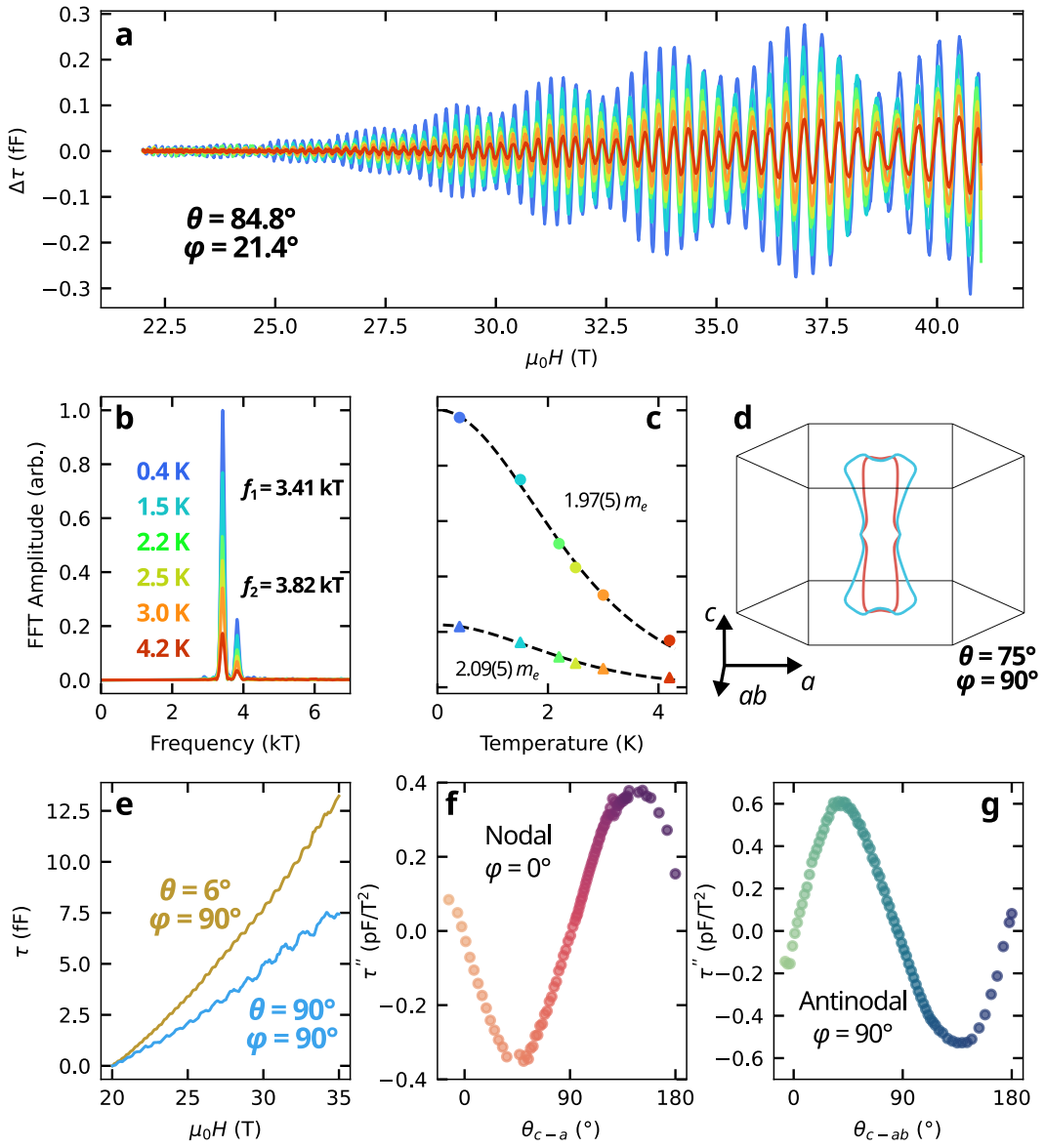


Fig. 4. Spin-split effective mass study. **a**, Quantum oscillations at incremental temperatures for $\theta = 84.8^\circ$, $\varphi = 21.4^\circ$ and **b**, their corresponding frequency spectra, with temperatures indicated. $\Delta\tau$ was high-pass filtered to focus on two frequency components, at $f_1 = 3.41$ kT and $f_2 = 3.82$ kT (see *Methods*), which come from spin-split up and down sheets of the primary dogbone Fermi surface. **c**, Temperature dependence of QO amplitude fitted to the Lifshitz-Kosevich formula,⁴⁰ yielding effective cyclotron masses of $m_1^* = 1.97(5) m_e$ and $m_2^* = 2.09(5) m_e$. The ratio of $\sqrt{f_1/f_2}$ is equal to that of m_1^*/m_2^* , as expected for these two frequency components being two spin-split daughters of the same mother Fermi sheet. **d**, Visualisation of the spin-up and spin-down orbits around the dogbone cross-section, which can enclose markedly different areas for the same field orientation. The effective cyclotron mass grows with increasing orbit area. **e**, Raw torque τ without background-subtraction at two orientations as indicated. Close to high-symmetry, the overall cantilever deflection is small, hence τ is dominated by the oscillatory component of magnetisation.

Fig. 4. (cont.) The raw torque for $\theta = \varphi = 90^\circ$ has been scaled by a factor of 5 so that its magnitude is comparable to that of the torque at $\theta = 6^\circ, \varphi = 90^\circ$. **f**, Second derivative of torque with respect to field, τ'' , for rotations in the nodal $c - a$ plane and **g**, in the antinodal $c - ab$ plane. Although the QO frequency profiles for these two planes are markedly different, with the loss of mirror symmetry for each spin-split frequency trace in the antinodal plane (Fig. 2e), the background magnetic torque still exhibits the higher symmetry representative of the crystal structure.

corroboration that these two frequencies may therefore be attributed to altermagnetic spin-splitting of the same parent sheet. The maximum spin-splitting can likewise be estimated from the frequency difference $\delta f = f_2 - f_1 = 0.41$ kT, which according to the Onsager relation³⁹ translates to a difference between the areas enclosed by spin-up and spin-down orbits as $\delta A = \delta f(2\pi e)/\hbar = \Delta \partial A / \partial \varepsilon = m^* \Delta (2\pi/\hbar^2)$, with Δ the energy splitting at the Fermi level. With the observed average effective mass $m^* \approx 2.03m_e$, we thereby estimate a spin-splitting at the Fermi level of $\Delta \approx 25$ meV for this field orientation.

Unconventional magnetic *g*-wave order parameter symmetry in CrSb

Putting together our results from measuring QOs upon rotating \mathbf{H} through the three different rotation planes presented in Figs. 2 & 3, we can firmly pin down the unconventional magnetic order parameter symmetry of CrSb. By tracking how the spin-split QO frequency profile of the primary CrSb Fermi pocket evolves under rotation, we identify four nodal planes in total: three defined for all θ at $\phi = 0^\circ, 60^\circ, 120^\circ$, and one for all ϕ at $\theta = 90^\circ$. We also note that $\theta = 0^\circ$ always lies on a ϕ -defined nodal plane. We can therefore compare the symmetry of our spin-split unconventional magnetic order parameter, $\Delta(\theta, \phi)$, to that of a real spherical harmonic. We find that $\Delta(\theta, \phi)$ obeys the symmetries of the real spherical harmonic $\mathcal{Y}_4^{-3}(\theta, \phi) \propto P_4^3(\cos \theta) \sin 3\phi$ defined in terms of the associated Legendre polynomial $P_\ell^m(x)$ ⁴¹ (see *Methods*). This harmonic transforms as the B_{1g} irreducible representation of the D_{6h} point group of CrSb. $\mathcal{Y}_4^{-3}(\theta, \phi)$ can be expressed in Cartesian form as $yz(3x^2 - y^2)$ or equivalently in spherical polars as

$r^4 \sin^3(\theta) \cos(\theta) \sin(3\phi)$ (sketched in Fig. 1f). This function has nodes when $\theta = 0^\circ, 90^\circ$ and $\phi = 0^\circ, 60^\circ, 120^\circ$, just as $\Delta(\theta, \phi)$ does. Our study thereby demonstrates that the sensitivity of QO measurements to spin-split band structures makes them an ideally suited diagnostic tool for ascertaining the order parameter symmetry of unconventional metallic magnets.

In summary, our systematic bulk-sensitive QO measurements have directly probed the unconventional magnetic order parameter symmetry of CrSb, revealing the g -wave altermagnetic spin texture. This manifests in the \vec{k} -dependence of the spin-splitting per Fermi pocket, $\Delta(\vec{k})$. For magnetic fields applied in highly symmetric nodal planes, $\Delta(\vec{k})$ is always zero. By contrast, rotating through arcs of low symmetry $\Delta(\vec{k})$ is generally large and well-resolvable, collapsing back to zero upon crossing through a nodal plane. For fields applied in nodal planes, quasi-particle orbits are spin-degenerate and mirror-symmetric. By contrast, in antinodal planes this mirror symmetry is lost, leading to spin-split QO frequency versus angle traces – providing a smoking-gun signature of altermagnetic ordering. These results thereby firmly establish CrSb as a room-temperature metallic altermagnet. Our optimised growth procedure has produced high-quality crystals with residual resistivities as low as $2 \mu\Omega\text{cm}$, making CrSb a promising candidate for exploring next-generation low-energy spintronic device applications.

References

1. Curie, P. *Propriétés magnétiques des corps à diverses températures* (Gauthier-Villers, Paris, 1895).
2. Heisenberg, W. Zur theorie des ferromagnetismus. *Z. Phys.* **49**, 619–636 (1928).
3. Bardeen, J., Cooper, L. N. & Schrieffer, J. R. Theory of Superconductivity. *Phys. Rev.* **108**, 1175–1204 (1957).
4. Stewart, G. R. Unconventional superconductivity. *Adv. Phys.* **66**, 75–196 (2017).
5. Jungwirth, T., Fernandes, R. M., Sinova, J. & Šmejkal, L. Altermagnets and beyond: Nodal magnetically-ordered phases (2024). URL <https://arxiv.org/abs/2409.10034>.
6. Liu, Q., Dai, X. & Blügel, S. Different facets of unconventional magnetism. *Nat. Phys.* **21**, 329–331 (2025).
7. Song, Q. *et al.* Electrical switching of a *p*-wave magnet. *Nature* **642**, 64–70 (2025).
8. Yamada, R. *et al.* A metallic *p*-wave magnet with commensurate spin helix. *Nature* **646**, 837–842 (2025).
9. Šmejkal, L., Sinova, J. & Jungwirth, T. Beyond Conventional Ferromagnetism and Antiferromagnetism: A Phase with Nonrelativistic Spin and Crystal Rotation Symmetry. *Phys. Rev. X* **12**, 031042 (2022).
10. Šmejkal, L., Sinova, J. & Jungwirth, T. Emerging Research Landscape of Altermagnetism. *Phys. Rev. X* **12**, 040501 (2022).
11. Hayami, S., Yanagi, Y. & Kusunose, H. Momentum-dependent spin splitting by collinear antiferromagnetic ordering. *J. Phys. Soc. Jpn.* **88**, 123702 (2019).
12. Šmejkal, L., González-Hernández, R., Jungwirth, T. & Sinova, J. Crystal time-reversal symmetry breaking and spontaneous Hall effect in collinear antiferromagnets. *Sci. Adv.* **6**, eaaz8809 (2020).
13. Ma, H.-Y. *et al.* Multifunctional antiferromagnetic materials with giant piezomagnetism and noncollinear spin current. *Nat. Commun.* **12**, 2846 (2021).
14. Shoenberg, D. *Magnetic Oscillations in Metals* (Cambridge University Press, Cambridge, UK, 1984). URL <https://doi.org/10.1017/CBO9780511897870>.
15. Song, C. *et al.* Altermagnets as a new class of functional materials. *Nat. Rev. Mater.* (2025).

16. Schrödinger, E. Quantisierung als Eigenwertproblem. *Ann. Phys.* **385**, 437–490 (1926).
17. Anderson, P. W. Plasmons, Gauge Invariance, and Mass. *Phys. Rev.* **130**, 439–442 (1963).
18. Higgs, P. W. Broken Symmetries and the Masses of Gauge Bosons. *Phys. Rev. Lett.* **13**, 508–509 (1964).
19. Leggett, A. J. A theoretical description of the new phases of liquid ^3He . *Rev. Mod. Phys.* **47**, 331–414 (1975).
20. Néel, L. Influence des fluctuations du champ moléculaire sur les propriétés magnétiques des corps. *Ann. Phys. (Fr.)* **17**, 5–105 (1932).
21. Shull, C. G. & Smart, J. S. Detection of Antiferromagnetism by Neutron Diffraction. *Phys. Rev.* **76**, 1256–1257 (1949).
22. Mazin, I. Editorial: Altermagnetism—A New Punch Line of Fundamental Magnetism. *Phys. Rev. X* **12**, 040002 (2022).
23. Fender, S. S., Gonzalez, O. & Bediako, D. K. Altermagnetism: A Chemical Perspective. *J. Am. Chem. Soc.* **147**, 2257–2274 (2025).
24. Wan, X., Mandal, S., Guo, Y. & Haule, K. High-Throughput Search for Metallic Altermagnets by Embedded Dynamical Mean Field Theory. *Phys. Rev. Lett.* **135**, 106501 (2025).
25. Hiraishi, M. *et al.* Nonmagnetic Ground State in RuO_2 Revealed by Muon Spin Rotation. *Phys. Rev. Lett.* **132**, 166702 (2024).
26. Keßler, P. *et al.* Absence of magnetic order in RuO_2 : insights from μSR spectroscopy and neutron diffraction. *npj Spintronics* **2**, 50 (2024).
27. Berlijn, T. *et al.* Itinerant Antiferromagnetism in RuO_2 . *Phys. Rev. Lett.* **118**, 077201 (2017).
28. Zhu, Z. H. *et al.* Anomalous Antiferromagnetism in Metallic RuO_2 Determined by Resonant X-ray Scattering. *Phys. Rev. Lett.* **122**, 017202 (2019).
29. Wu, Z. *et al.* Fermi Surface of RuO_2 Measured by Quantum Oscillations. *Phys. Rev. X* **15**, 031044 (2025).
30. Li, Z.-X., Zhou, H., Wan, X. & Chen, W. Diagnosing altermagnetic phases through quantum oscillations. *Phys. Rev. B* **111**, 125119 (2025).
31. Huang, Y. *et al.* Ab initio study of quantum oscillations in altermagnetic and nonmagnetic phases of RuO_2 . *Phys. Rev. B* **110**, 144410 (2024).

32. Liu, J. *et al.* Absence of Altermagnetic Spin Splitting Character in Rutile Oxide RuO₂. *Phys. Rev. Lett.* **133**, 176401 (2024).
33. Osumi, T. *et al.* Spin-Degenerate Bulk Bands and Topological Surface States of RuO₂ (2025). URL <https://arxiv.org/abs/2501.10649>. arXiv:2501.10649.
34. Willis, B. Crystal structure and antiferromagnetism of CrSb. *Acta Crystallogr.* **6**, 425–426 (1953).
35. Snow, A. I. Neutron Diffraction Investigation of the Atomic Magnetic Moment Orientation in the Antiferromagnetic Compound CrSb. *Phys. Rev.* **85**, 365–365 (1952).
36. Yang, G. *et al.* Three-dimensional mapping of the altermagnetic spin splitting in CrSb. *Nat. Commun.* **16**, 1442 (2025).
37. Singh, A. K. *et al.* Chiral Spin-Split Magnons in the Metallic Altermagnet CrSb (2025). URL <https://arxiv.org/abs/2511.16086>.
38. Kramers, H. Théorie générale de la rotation paramagnétique dans les cristaux. *Proc. Amsterdam Akad* **33**, 959–972 (1930).
39. Onsager, L. Interpretation of the de Haas-van Alphen effect. *Philos. Mag.* **43**, 1006–1008 (1952).
40. Lifshitz, I. M. & Kosevich, A. M. Theory of Magnetic Susceptibility in Metals at Low Temperatures. *Sov. Phys. JETP* **2**, 636–645 (1956).
41. Blanco, M. A., Flórez, M. & Bermejo, M. Evaluation of the rotation matrices in the basis of real spherical harmonics. *Journal of Molecular Structure: THEOCHEM* **419**, 19–27 (1997).
42. Eaton, A. G. *et al.* Quasi-2D Fermi surface in the anomalous superconductor UTe₂. *Nat. Commun.* **15**, 223 (2024).
43. Cleveland, W. S. & Devlin, S. J. Locally weighted regression: An approach to regression analysis by local fitting. *J. Am. Stat. Assoc.* **83**, 596–610 (1988).
44. Blaha, P. *et al.* WIEN2k: An APW+lo program for calculating the properties of solids. *J. Chem. Phys.* **152**, 074101 (2020).
45. Rourke, P. & Julian, S. Numerical extraction of de Haas–van Alphen frequencies from calculated band energies. *Comput. Phys. Commun.* **183**, 324–332 (2012).
46. Weinberger, T. Py_FS, GitHub repository [https://github.com/TheoWeinberger/py_FS] (2023). URL https://github.com/TheoWeinberger/py_FS.

47. Altarawneh, M. M., Mielke, C. H. & Brooks, J. S. Proximity detector circuits: An alternative to tunnel diode oscillators for contactless measurements in pulsed magnetic field environments. *Rev. Sci. Instrum.* **80**, 066104 (2009).
48. Wu, Z. *et al.* Enhanced triplet superconductivity in next-generation ultraclean UTe₂. *Proc. Natl. Acad. Sci. USA* **121**, e2403067121 (2024).

Methods

Crystal growth

Single crystal CrSb specimens were grown by the chemical vapour transport technique. Stoichiometric amounts of Cr (chunks, 99.995%) and Sb (Shots, 99.9999%) were used as source material. Iodine was added as a transport agent, calculated to have a pressure of 1 bar at growth conditions. The starting materials were sealed under vacuum in a quartz ampule and placed in a horizontal two-zone furnace. The temperature was slowly ramped up to $T_1 = 925$ °C and $T_2 = 900$ °C, left for two weeks, and subsequently cooled at the furnace cooling rate to room temperature. The resulting crystals were hexagonal platelets up to 1.5 mm in diameter, along with larger areas possessing intergrown crystals of CrSb, several mm in size. Only single-crystal specimens were used in this study.

Sample characterisation

Several crystals were picked from a batch of single crystals and crushed into a fine powder. This powdered sample was then distributed on a microscope slide, which had a thin layer of vacuum grease. Powder X-ray diffraction was measured in the Bragg-Brentano geometry on a Bruker D8, using a Cu-source, with the results plotted in Extended Data Fig. 1. The measurement was performed in a 2θ range of 10° - 90°, with no peaks observed below 20°.

The obtained data display sharp, well-defined peaks, indicating a high level of crystallinity. The data were analysed using the Rietveld method, yielding an excellent fit ($R_{\text{Bragg}} = 3.39$), which describes all observed peaks, thereby indicating that the samples are phase pure. The measured crystal structure is in good agreement with prior studies.³⁴

We also performed electrical transport, magnetisation, and Laue diffractometry measurements (Extended Data Fig. 1). Samples were predominantly screened by temperature-dependent resistivity measurements, utilised to extract their residual resistivity ratios (RRRs). To do this, we fitted the low-temperature data to the square of the temperature and extrapolated to absolute zero to determine the residual resistivity. The 300 K resistivity was then divided by this value to yield the RRR. Higher RRR values indicate longer mean free paths and hence higher crystalline quality. Typical RRR values were in the approximate range of 10-28. High-quality specimens were then oriented by Laue diffractometry, in preparation for high magnetic field dHvA measurements.

de Haas-van Alphen effect torque magnetometry measurements

High-quality samples were selected following characterisation screening and brought to the

National High Magnetic Field Laboratory (NHMFL), Tallahassee, Florida, USA. For torque magnetometry measurements, we largely followed the methodology outlined in ref.⁴² Samples were mounted on flexible BeCu cantilevers and affixed using multiple layers of General Electric low-temperature varnish, giving good thermal contact and strong adhesion between sample and cantilever. Cantilevers were soldered in place, such that the cantilever head was suspended above a copper baseplate, by a short separation distance. As the magnetic field was swept, the change in capacitance between the cantilever and baseplate, due to the magnetic torque exerted on the sample, was measured by a General Radio Analogue capacitance bridge using phase-sensitive detection. The change in torque was calibrated to units of Farads using an Andeen Hagerling digital capacitance bridge.

All dHvA measurements were performed in the 41.5 T all-resistive magnet in Tallahassee. A ³He sample environment was utilised, along with a probe mounting of our custom design. Rotations of the sample orientation with respect to the magnetic field were performed *in-situ* utilising a brushless linear motor. Angles were calibrated by the change in sign of the torque background – identifying high symmetry directions of the crystal – and verified using a Hall sensor.

The oscillatory component $\Delta\tau$ was isolated from the background magnetic torque τ by performing a LOESS⁴³ subtraction. In general, due to the intricate web sheet of the CrSb Fermi surface, the dHvA waveform at a given angle could be quite complicated due to the presence of numerous frequency components. To simplify our analysis and concentrate on the dogbone Fermi sheet, we often performed combined high-pass filtering with short LOESS windows throughout our analysis. The dogbone frequencies are most prominent above 3 kT, and so we Butterworth high-pass filtered frequencies in inverse field in this range. This was combined with a short sliding LOESS window over τ , which effectively fits any slow oscillations in with the background (always assumed to be quadratic in H), therefore producing a $\Delta\tau$ waveform dominated by higher frequency components. For the $\Delta\tau$ traces presented in Fig. 1, this involved using a LOESS window of 0.7 T. In Fig. 2, we used a window of length 1.2 T to show the strong spectral weight at lower frequencies due to the web. By contrast, in Fig. 4 we utilised a window of only 0.6 T to focus on the > 3 kT components in our temperature dependence study.

Density functional theory calculations

Density functional theory (DFT) calculations for CrSb were performed using the all-electron, full-potential linearised augmented plane-wave (FP-LAPW) method as implemented in the WIEN2k code.⁴⁴ The electronic structure was converged on a $43 \times 43 \times 28$ Monkhorst–Pack k -point mesh within the Brillouin zone of the primitive hexagonal unit cell. Exchange–correlation effects were treated within the Generalised Gradient Approximation (GGA). We specified two distinct Cr sites (Cr₁ and Cr₂) within the primitive unit cell, corresponding to Cr atoms adopting up and down spin polarisation. Calculations were initialised so that one Cr site has a higher spin-up density and the other has a spin-down density. The onsite spin-polarisation was then allowed to vary throughout the self-consistency cycles until the compensated collinear ground state was reached. Quantum oscillation frequency analysis of the resultant Fermi surface sheets

was determined using SKEAF.⁴⁵ Fermi surface visualisation was performed using py_FS.^{42,46}

We assumed that ambient pressure CrSb in the NiAs-type structure ($P6_3/mmc$) adopts lattice parameters $a = 4.12$ Å, $b = 4.12$ Å, and $c = 5.47$ Å. Within the unit cell, there are two equivalent Cr sites:

Atom	X	Y	Z
Cr ₁	0.00	0.00	0.00
Cr ₂	0.00	0.00	0.50

and two equivalent Sb sites:

Atom	X	Y	Z
Sb ₁	0.67	0.33	0.25
Sb ₂	0.33	0.67	0.75

We reduce the symmetry of the crystal lattice from $P6_3/mmc$ to $P3m1$ by specifying that the two Cr sites adopt opposite spins.

DFT calculations converge on a Fermi surface where the bands associated with the down and up ‘dogbone’ surfaces are open about the A high symmetry point, corresponding to a cylindrical topology. This is inconsistent with our quantum oscillation measurements, where we resolve oscillations from these sheets for magnetic fields along the a and ab axes. No frequencies would be observed for these field orientations if the sheets were cylindrical. Therefore, we propose that these bands form closed Fermi surface sheets with dogbone-like geometry. To ‘close’ the open Fermi surface sheets of our DFT calculations, we shift our band edges relative to the Fermi energy. The dogbone-like sheets were shifted down by 0.11 eV so that the calculated frequencies along the a , ab , and c -directions are in good agreement with the quantum oscillation data. Since the dogbone sheets are of hole-character, we shifted up the ‘web’ sheets (of electron-character) by 0.015 eV to keep the total carrier number constant.

Energy Splitting from Quantum Oscillation Frequencies

From the Onsager relation, we can equate a quantum oscillation frequency to a reciprocal space area as

$$F(E) = \frac{\hbar}{2\pi e} A(E) \quad (1)$$

The cyclotron mass of an orbit, m_c , is related to the rate of change of the orbital area by

$$m_c = \frac{\hbar^2}{2\pi} \frac{\partial A}{\partial E} \Big|_{E_f} \quad (2)$$

By taking the derivative of Eq. 1 with respect to E we then determine

$$\frac{dF}{dE} = \frac{\hbar}{2\pi e} \frac{\partial A}{\partial E} = \frac{\hbar}{2\pi e} \frac{2\pi}{\hbar^2} m_c = \frac{m_c}{e\hbar} \quad (3)$$

We can use this to determine the energy difference associated with the frequency splitting of two bands

$$\Delta E \sim \Delta F \frac{dE}{dF} = \frac{e\hbar}{m_c} \Delta F \quad (4)$$

Spherical Harmonic Notation

In the text, we represent the symmetry of the altermagnetic spin-splitting of CrSb in terms of the real spherical harmonic $\mathcal{Y}_4^{-3}(\theta, \phi)$.

The complex spherical harmonics can be defined in terms of the associated Legendre Polynomials as $Y_\ell^m(\theta, \phi) = N_{\ell m} e^{im\phi} P_\ell^m(\cos \theta)$, where $N_{\ell m}$ is a normalisation factor, $P_\ell^m(x)$ is an associated Legendre polynomial, and $Y_\ell^m(\theta, \phi)$ is the complex spherical harmonic for $\ell \geq 0$ and $m \in [-\ell, \ell]$. The complex spherical harmonics are eigenfunctions of the total angular momentum operator \hat{L}^2 and of the generator of rotations about the azimuthal axis \hat{L}_z , spanning a complete orthonormal basis.

The complex spherical harmonics are defined up to a phase factor $e^{im\phi}$, and so their magnitude does not change as a function of ϕ . Therefore, it is convenient to work in the basis of the real spherical harmonics, which have explicit ϕ dependence, when describing the symmetry of our unconventional magnetic order parameter. We can define the real spherical harmonics $\mathcal{Y}_\ell^m(\theta, \phi)$ in terms of linear combinations of complex harmonics according to:

$$\mathcal{Y}_\ell^m = \begin{cases} \frac{1}{\sqrt{2}} (Y_\ell^{-m} + (-1)^m Y_\ell^m) & \text{if } m > 0 \\ Y_\ell^0 & \text{if } m = 0 \\ \frac{i}{\sqrt{2}} (Y_\ell^{-|m|} - (-1)^{|m|} Y_\ell^{|m|}) & \text{if } m < 0, \end{cases} \quad (5)$$

or equivalently, in terms of the associated Legendre polynomials:

$$\mathcal{Y}_\ell^m = \begin{cases} \sqrt{2}(-1)^m N_{\ell m} P_\ell^m(\cos \theta) \cos(m\phi) & \text{if } m > 0 \\ N_{\ell 0} P_\ell^0(\cos \theta) & \text{if } m = 0 \\ \sqrt{2}(-1)^m N_{\ell|m|} P_\ell^{|m|}(\cos \theta) \sin(|m|\phi) & \text{if } m < 0. \end{cases} \quad (6)$$

Defining the real spherical harmonics this way means they form a complete set that spans the same basis as the complex spherical harmonics; however, importantly they have well-defined,

varying magnitudes as a function of ϕ . This allows us to map the \mathcal{Y}_4^{-3} real spherical harmonic to the g -wave symmetry profile of the altermagnetic order parameter in CrSb.

Contactless resistivity measurements

Contactless resistivity measurements were conducted using the proximity detector oscillator⁴⁷ (PDO) technique. A selected CrSb sample was mounted on a hand-wound planar coil of 15 turns, acting as the inductive component of the oscillator. The coil diameter was customised to match the sample width for optimal filling factor. A counter-wound outer coil enclosing the same area as the inner coil was added to compensate magnetic flux induced during the field pulse, minimising background pickup.

As the applied magnetic field is swept, changes in the sample's resistivity ρ and susceptibility χ_s lead to changes in the inductance of the oscillator and produce a shift in the resonant frequency of the oscillator, which can be described by

$$\frac{\Delta f}{f} \approx -\eta \frac{\delta}{d} \left(\mu_r \frac{\Delta \rho}{\rho} + \Delta \chi_s \right), \quad (7)$$

where η is the filling factor, d is the sample thickness, and $\mu_r = 1 + \chi_s$ is the relative magnetic permeability. For a metallic material like CrSb, eddy current restricts the penetration of the RF field to a characteristic skin depth $\delta = \sqrt{2\rho/(\mu_r \mu_0 \omega)}$, where ω is the excitation frequency, such that the frequency response is dominated by changes in the resistivity ρ .

PDO measurements reported in this study were performed in a 65 T pulsed magnet at the Dresden High Magnetic Field Laboratory (HLD) in Dresden, Germany, following the methodology of ref.⁴⁸ A customised ³He cryostat was fitted to the magnet, providing a base temperature of \sim 600 mK throughout the pulses. A raw resonant frequency \sim 25 MHz was achieved, followed by a heterodyne mixing circuit to down-convert the signal to \sim 10.5 MHz, which was subsequently acquired using a high definition oscilloscope.

Quantum oscillatory components were analysed over a magnetic field range of 38 – 63 T using a LOESS background subtraction with an 8 T window and a second-order polynomial background subtraction. A quantum oscillation of frequency 0.8 kT was clearly resolved (Extended Data Fig. 7).

Acknowledgements

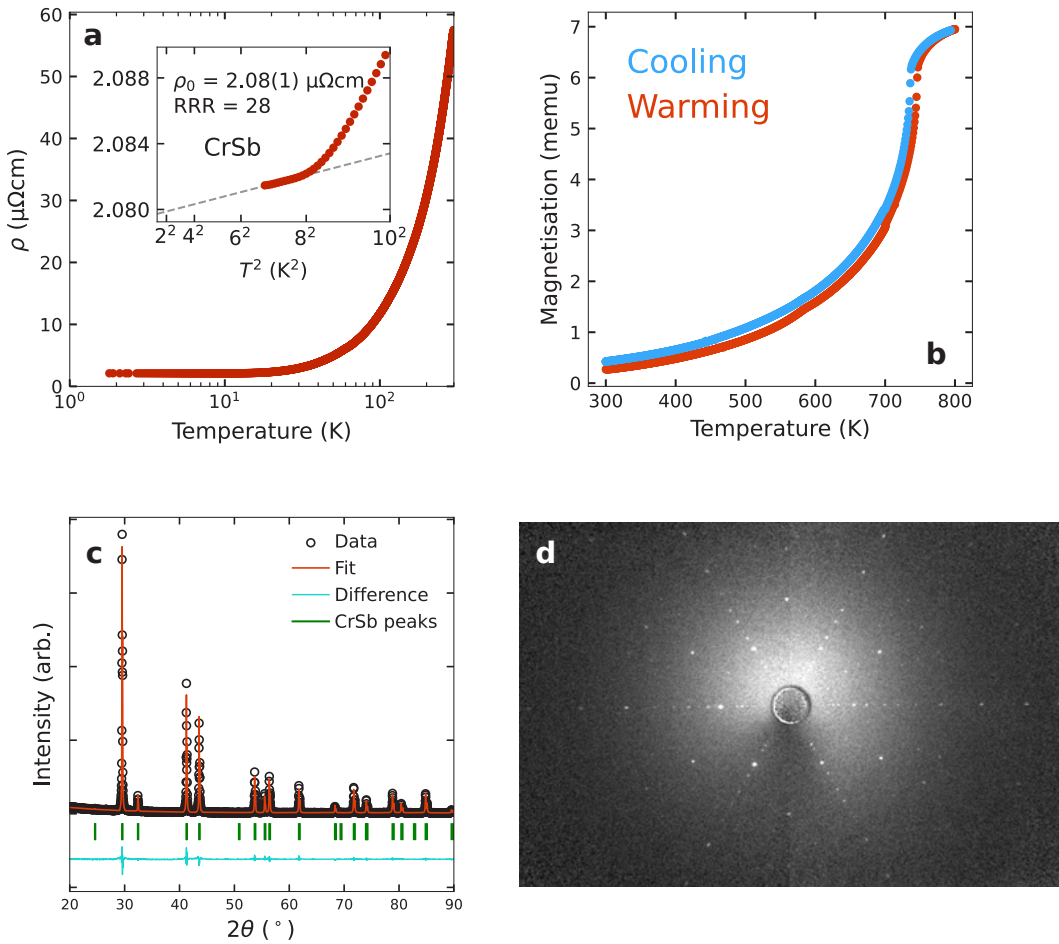
We are grateful to A.J. Hickey, A. Agarwal, T.L. Lefebvre and N.J.M. Popiel for stimulating discussions. We thank T. Haidamak, M. Vališka, H. Li, P. Einarsson Nielsen, H. Chen, R. Mann, T.J. Brumm, and especially D. Sviták and S. Hayden, for technical advice and assistance. We appreciate creative input from H. Weinberger. This project was supported by the EPSRC of the UK through grants EP/X011992/1 and EP/R513180/1. A portion of this work was performed at the National High Magnetic Field Laboratory, which is supported by National Science Foundation Cooperative Agreement Nos. DMR-1644779 & DMR-2128556 and the State of Florida. We acknowledge support of the HLD at HZDR, a member of the European Magnetic Field Laboratory (EMFL). T.I.W. and A.G.E. acknowledge support from ICAM through US National Science Foundation (NSF) Grant Number 2201516 under the Accelnet program of the Office of International Science and Engineering and from QuantEmX grants from ICAM and the Gordon and Betty Moore Foundation through Grant GBMF9616. T.I.W. acknowledges support from Murray Edwards College (University of Cambridge) and the Cambridge Philosophical Society through a Henslow Fellowship. A.G.E. acknowledges support from Sidney Sussex College (University of Cambridge).

Data availability

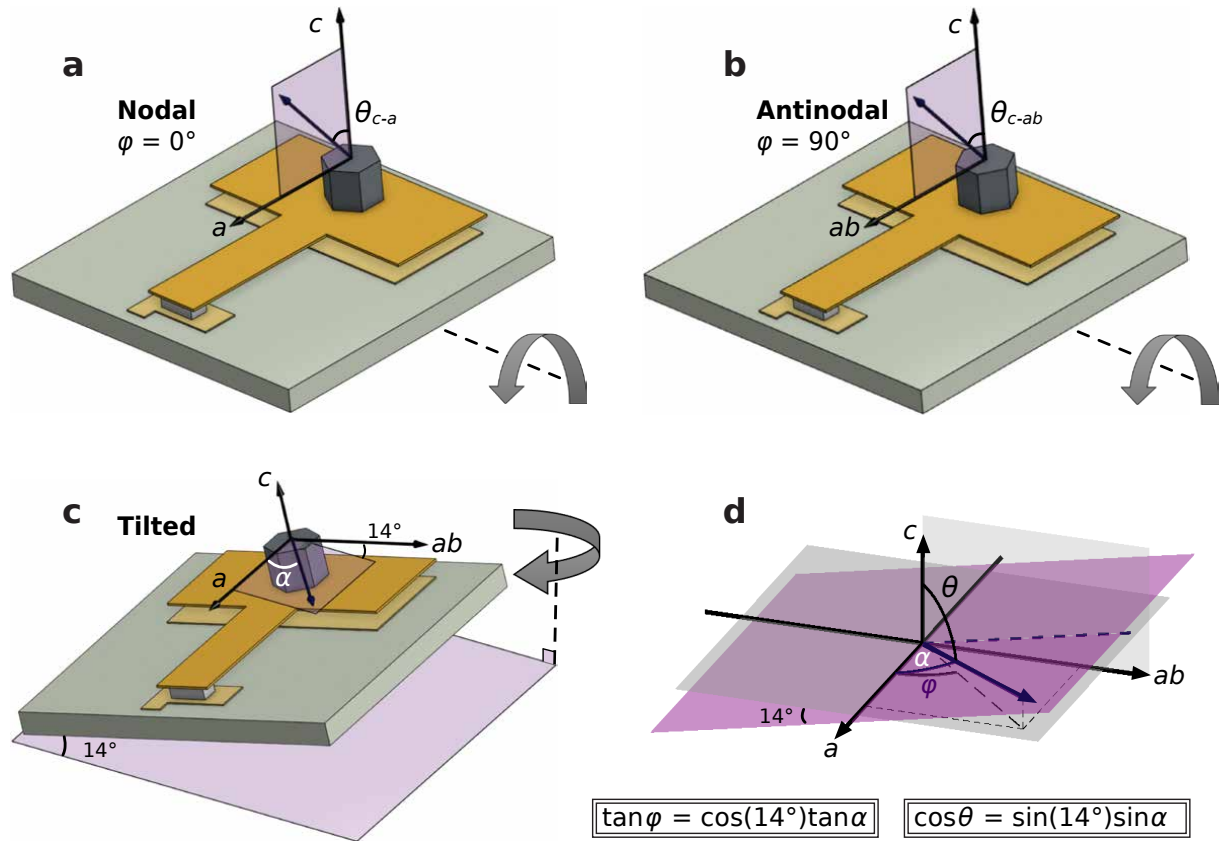
The datasets supporting the findings of this study will be uploaded to the University of Cambridge Apollo Repository prior to publication.

Competing interests statement

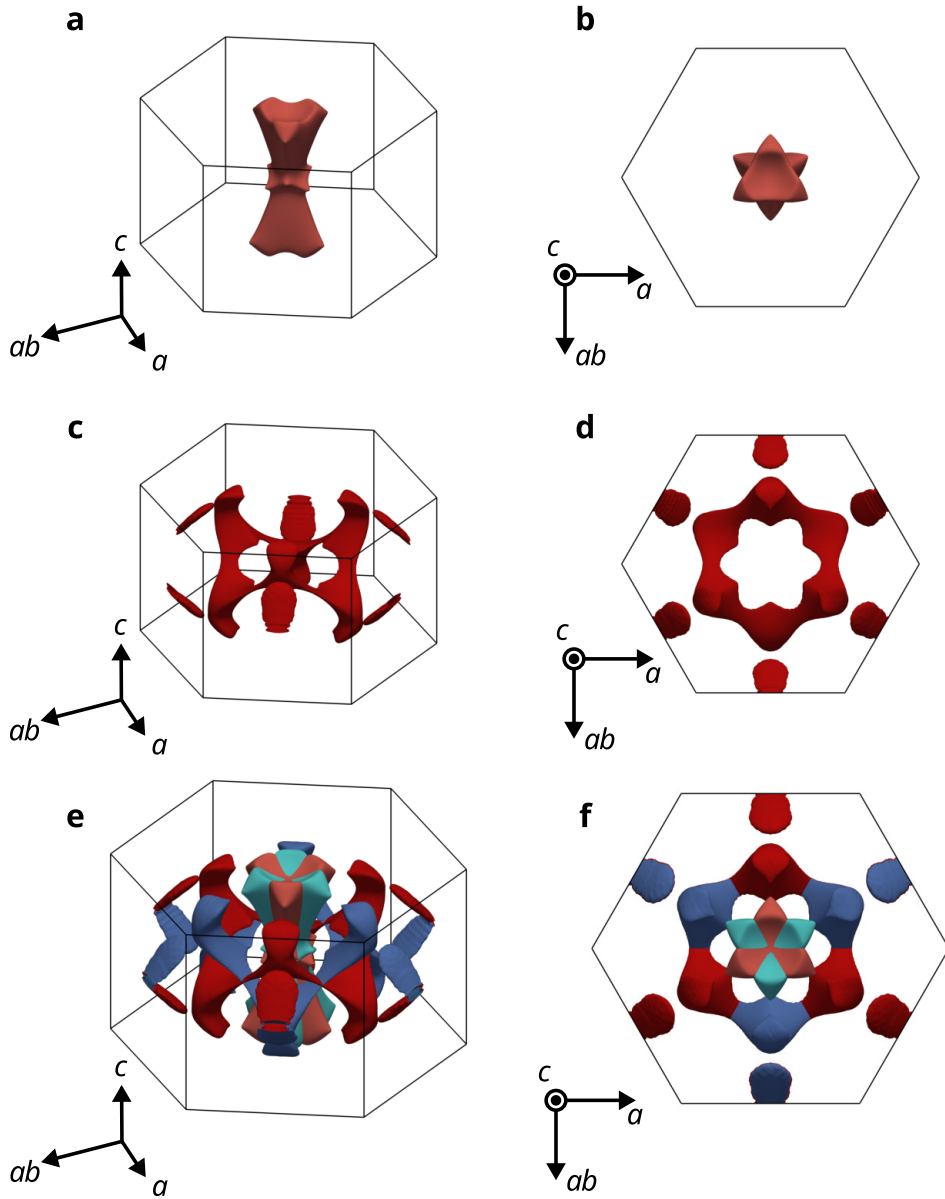
The authors declare no competing interests.



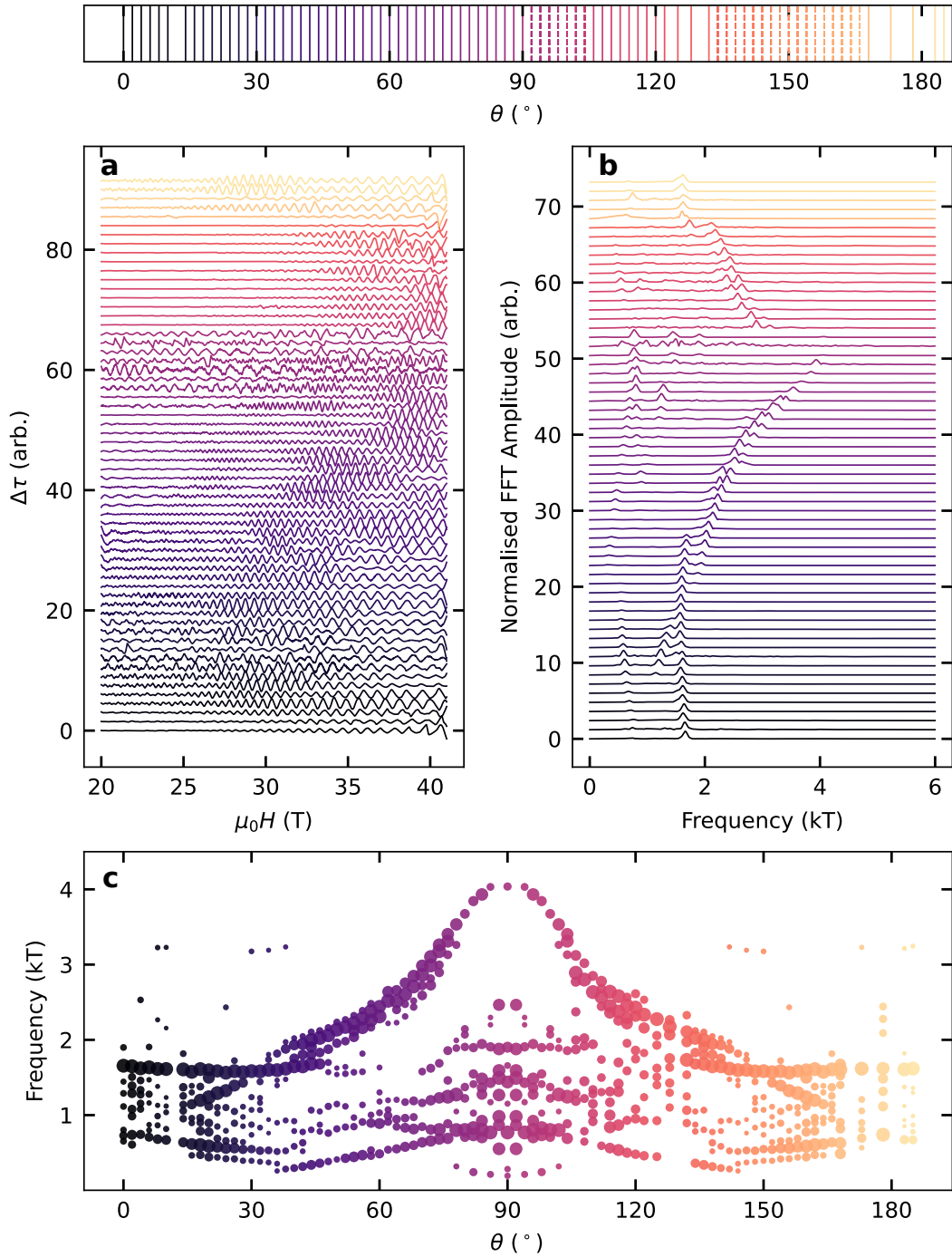
Extended Data Fig. 1 — Sample characterisation studies. **a**, Electrical resistivity ρ of CrSb measured by the four-terminal technique. The inset shows low temperature data fitted quadratically in temperature, to extract the residual resistivity of $2.08(1) \mu\Omega\text{cm}$. This yields a residual resistivity ratio, upon dividing the 300 K resistivity by the fitted extrapolation to absolute zero, of $\text{RRR} = 28$. **b**, Magnetisation versus temperature up to 800 K, measured in a Quantum Design Magnetic Properties Measurement System with the furnace option mode. Red points were recorded on warming, with blue taken subsequently upon cooling. An anomaly at ≈ 740 K is resolved, indicating the onset of compensated collinear magnetic order. This is slightly higher than previously reported,³⁵ likely due to improved crystal quality. **c**, Powder x-ray diffraction data plotted versus 2θ . The recorded data agree very well with the known structure³⁴ of CrSb. **d**, Lauegram of a single crystal specimen utilised in our quantum oscillation study. Sharp spots in a hexagonal pattern are clearly resolved, confirming single-crystallinity.



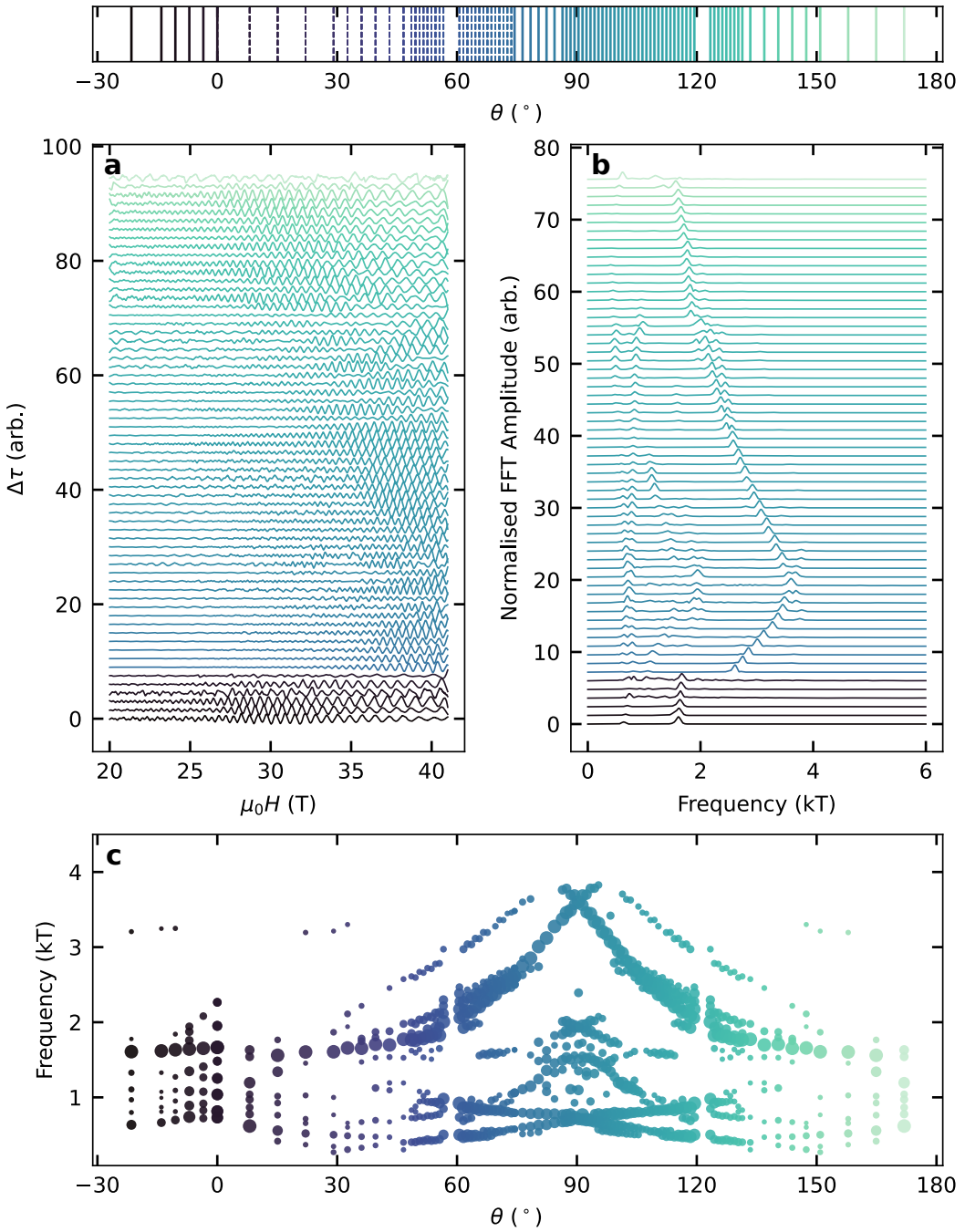
Extended Data Fig. 2 — Schematic diagrams of the rotational planes measured in this study. **a**, The relative crystal orientation with respect to the rotation axis for the nodal $c - a$ rotation plane and **b**, the same for the antinodal $c - ab$ plane. The dark grey hexagonal prism depicts the sample, which is mounted on a metallic cantilever narrowly suspended above a copper baseplate, therefore enabling capacitive torque magnetometry measurements. **c**, The tilted rotation plane for which data are presented in Fig. 3, for which the relative orientations of θ and φ with respect to α are defined in **d**.



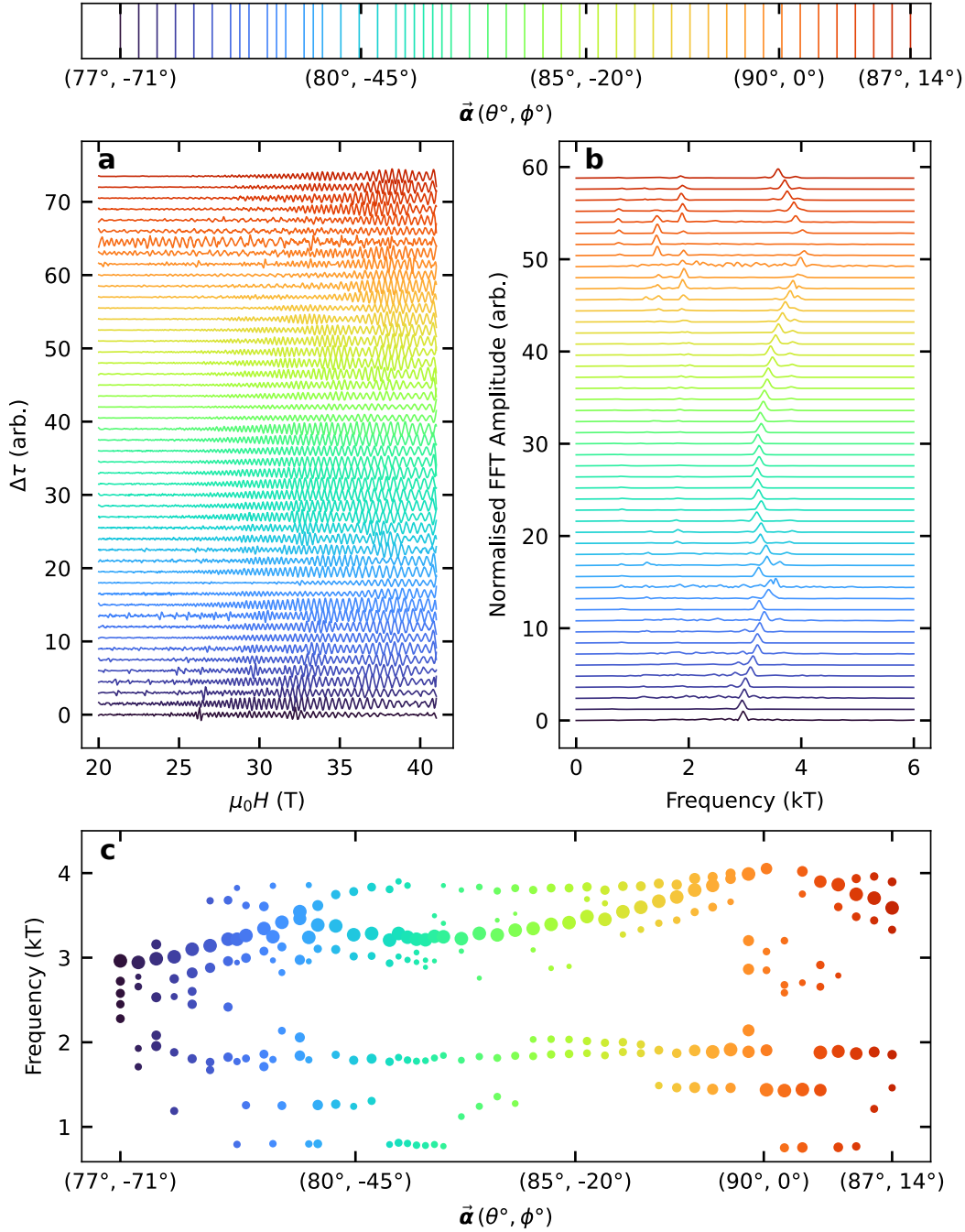
Extended Data Fig. 3— Fermi surface renderings. **a,b,** The principal (dogbone) Fermi sheet due to two hole-type bands that cross the Fermi level, and **c,d,** the secondary (web) sheet that results from two electron-type sheets crossing the Fermi level. For clarity, we plot only the up-sheets here. **e,f** Spin-up (red) and spin-down (blue) sheets of the entire Fermi surface of CrSb.



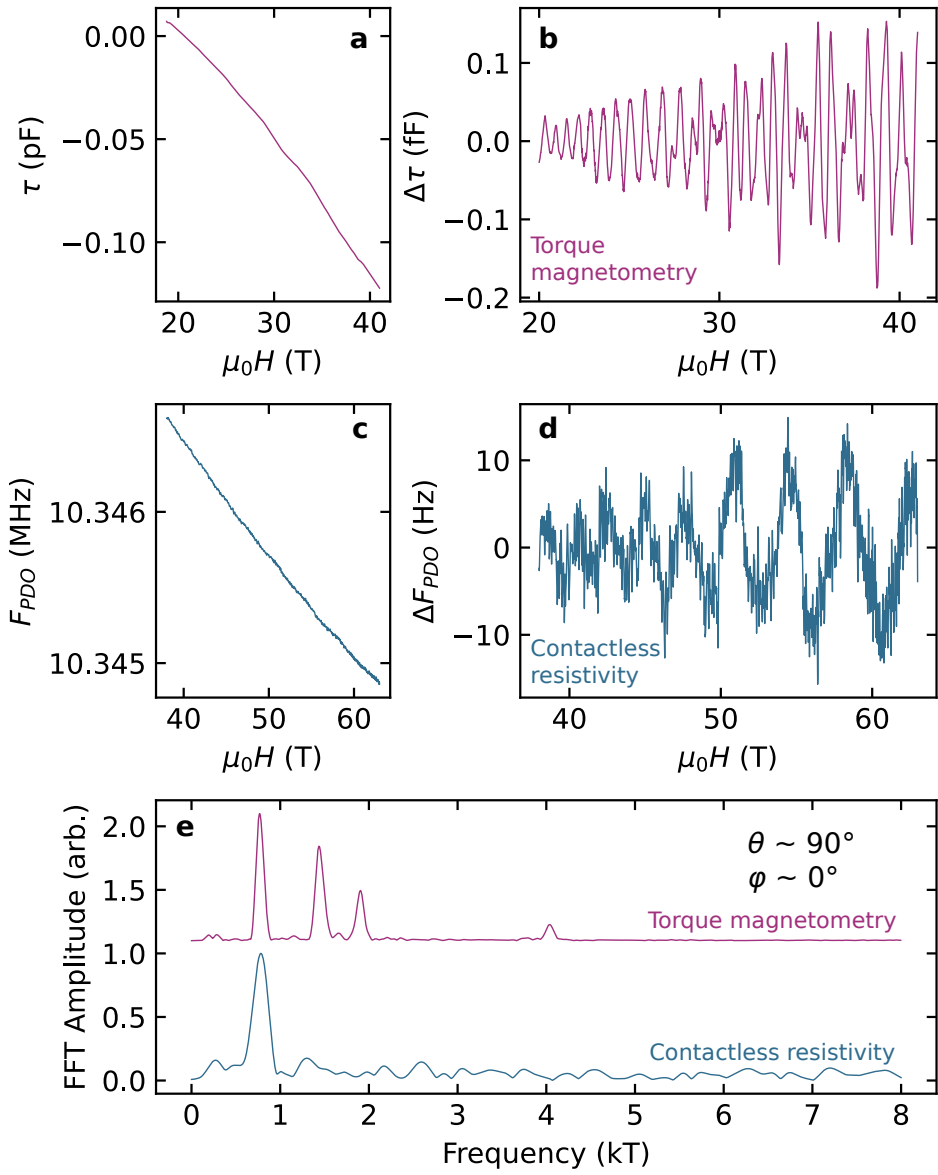
Extended Data Fig. 4 — Quantum oscillation measurements in the nodal $c - a$ rotation plane. **a**, Normalised oscillatory component of magnetic torque $\Delta\tau$, **b**, the corresponding fast Fourier transform spectra, and **c**, the frequency versus angle profile. A magnetic field range of 20–41 T was used, along with a LOESS window of 1.2 T and a second-order polynomial (see *Methods*). Dashed lines in the angular scale bar denote where symmetry-equivalent traces have been reflected through $\theta = 90^\circ$, for display purposes in panel **c**. No spin-splitting is resolved in this nodal plane.



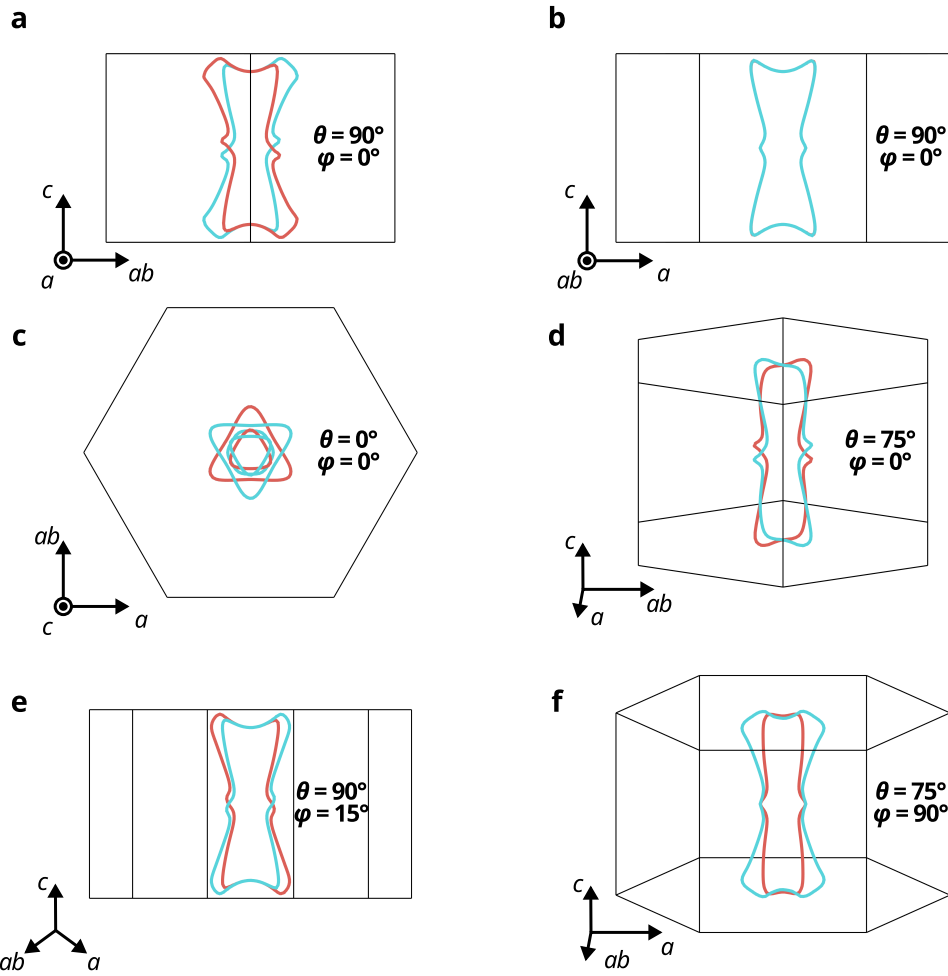
Extended Data Fig. 5 — Quantum oscillation measurements in the antinodal $c - ab$ rotation plane. **a**, Normalised oscillatory component of magnetic torque $\Delta\tau$, **b**, the corresponding fast Fourier transform spectra, and **c**, the frequency versus angle profile. A magnetic field range of 20–41 T was used, along with a LOESS window of 1.2 T and a second-order polynomial (see *Methods*). Dashed lines in the angular scale bar denote where symmetry-equivalent traces have been reflected through $\theta = 90^\circ$, for display purposes in panel **c**. Significant spin-splitting is resolved close to $\theta = 90^\circ$, as shown clearly in Fig. 2.



Extended Data Fig. 6 — Quantum oscillation measurements in a low-symmetry tilted rotation plane. **a**, Normalised oscillatory component of magnetic torque $\Delta\tau$, **b**, the corresponding fast Fourier transform spectra, and **c**, the frequency versus angle profile. A magnetic field range of 20–41 T was used, along with a LOESS window of 0.6 T and a second-order polynomial (see *Methods*). The rotation plane is defined in Extended Data Fig. 2. The high frequency branch undergoes significant spin-splitting away from nodal planes, as shown clearly in Fig. 3.



Extended Data Fig. 7 — Pulsed magnetic field QO measurements. **a**, Capacitive torque magnetometry measured in steady fields and **b**, the background-subtracted oscillatory profile. **c**, Contactless resistivity measured by the PDO technique (see *Methods*) in pulsed fields and **d**, the background-subtracted oscillatory profile. **e**, FFT traces for both measurements, performed with the same magnetic field orientation. The signal-to-noise ratio of the contactless resistivity is insufficient to resolve the high frequency components, however the peak at 0.8 kT is well resolved. This frequency branch appears robust, with no sign of a Lifshitz transition, at least up to 64 T.



Extended Data Fig. 8 — Comparison of orbital areas for different magnetic field orientations. **a**, Orienting magnetic field along the a -axis lies within a nodal plane, therefore the orbit for up-spins (red) can be mirrored through this plane onto a down-spin orbit. The result is that although the two orbits follow different paths in space, they are degenerate in area. Conversely, applying fields along the **b**, ab -direction or **c**, c -direction induces quasiparticle orbits that are parallel to these nodal planes. If the up/down orbits lie in the nodal planes, they are truly degenerate in shape. If they lie above the planes, they can be mirrored to a matching orbit of the opposite spin below the plane. Magnetic fields applied within the **d**, $c - a$ and **e**, $a - ab$ planes lie along nodal directions. This produces orbits that follow different paths depending on the spin direction but are degenerate in area. **f**, When the field is applied away from a nodal direction, but is not perpendicular to a nodal plane, we cannot use the ‘reflective’ symmetry that spin orbits hold about nodal planes to map up-spin orbits to down-spin orbits of equal area. Instead, quasiparticles orbiting around up- and down-sheets follow different paths of different areas. This results in QOs of different frequencies, due to altermagnetic band splitting.